Title	Predicting the elastic properties of selective laser sintered PCL/b-TCP bone scaffold materials using computational modelling.
Author(s)	Doyle, Heather; Lohfeld, Stefan; McHugh, Peter E.
Publication Date	2013
Publication Information	Doyle, H., Lohfeld, S., McHugh, P.E. (2013) 'Predicting the elastic properties of selective laser sintered PCL/b-TCP bone scaffold materials using computational modelling'. Annals Of Biomedical Engineering, 42 (3):661-677.
Publisher	Springer
Link to publisher's version	http://link.springer.com/article/10.1007%2Fs10439-013-0913-4
Item record	http://hdl.handle.net/10379/5524
DOI	http://dx.doi.org/10.1007/s10439-013-0913-4

Accepted manuscript, published in *Annals of Biomedical Engineering* 09/2013; 42(3), pp 661-677.
The final publication is available at Springer via http://dx.doi.org/10.1007/s10439-013-0913-4

Title: Predicting the elastic properties of selective laser sintered PCL/β-TCP bone scaffold materials using computational modelling.

Abbreviated Title: Predicting elastic properties of sintered scaffold materials

Author Names: Heather Doyle[a]; Stefan Lohfeld, Dr.[a]; Peter McHugh, Prof.[a]

Author Affiliations: [a]Biomechanics Research Centre (BMEC), Mechanical and Biomedical Engineering, National University of Ireland, Galway

Corresponding Author: Heather Doyle
Biomechanics Research Centre (BMEC)

Mechanical and Biomedical Engineering

College of Engineering and Informatics
National University of Ireland Galway
Galway, Ireland
Tel: +353 (0)91 493020
Fax: +353 (0)91 563991
Email: h.doyle1@nuigalway.ie

1 Abstract

This study assesses the ability of finite element models to capture the mechanical behaviour of sintered orthopaedic scaffold materials. Individual scaffold struts were fabricated from a 50:50 wt% poly-ε-caprolactone (PCL) /β-tricalcium phosphate (β-TCP) blend, using selective laser sintering (SLS). The tensile elastic modulus of single struts was determined experimentally. High resolution finite element models of single struts were generated from micro-CT scans (28.8μm resolution) and an effective strut elastic modulus was calculated from tensile loading simulations. Three material assignment methods were employed: (1) homogeneous PCL elastic constants, (2) composite PCL/ β-TCP elastic constants based on rule of mixtures, and (3) heterogeneous distribution of micromechanically-determined elastic constants. In comparison with experimental results, the use of homogeneous PCL properties gave a good estimate of strut modulus; however it is not sufficiently representative of the real material as it neglects the β-TCP phase. The rule of mixtures method significantly overestimated strut modulus, while there was no significant difference between strut modulus evaluated using the micromechanically-determined elastic constants and experimentally evaluated strut modulus. These results indicate that the multi-scale approach of linking micromechancial modelling of the sintered scaffold material with macroscale modelling gives an accurate prediction of the mechanical behaviour of the sintered structure.

Keywords: selective laser sintering; polycaprolactone, B-tricalcium phosphate; micromechanical modelling; bone tissue engineering; mechanical properties; finite element analysis.

2 Introduction

The purpose of bone tissue engineering scaffolds is to fill defects and support mechanical loading while providing a template on which new bone will form. The remodelling of native bone in response to mechanical loading occurs when cells convert mechanical stimuli to chemical signals to direct the formation of new tissue or resorption through mechanotransduction[30,44]. The mechanical stimuli that influence bone formation in vivo are a combination of both fluid shear over the cells[36,55] and mechanical loading of the cells[16,24,58], therefore it is important to be able to accurately predict the mechanical behaviour of bone tissue engineering scaffolds. In this study, methods are developed to capture the local stiffness of complex sintered scaffold materials. These properties are then used in combination with high resolution models that capture the real scaffold geometry and microstructure to predict the macroscale scaffold stiffness.

In this study, we focus on bone scaffold material fabricated poly-ε-caprolactone (PCL) and β-tricalcium phosphate (β-TCP) using selective laser sintering (SLS). While there is debate over whether soft or stiff scaffolds are more suitable for bone formation in vivo, here we consider the case of relatively stiff scaffolds for application in bridging critical sized defects in large bones as per Lohfeld et al.[34] that require the scaffold to support high levels of mechanical loading. The accurate knowledge and prediction of the overall mechanical properties, in particular the overall elastic modulus of the scaffold, is of considerable importance to the scaffold developer, and is the primary focus of the present work.

PCL is a bioresorbable, biocompatible polymer with a slow degradation time (>2 years[17,37]) that is easily processed with a melt temperature of 55-60°C and a glass transition temperature of -60°C[60]. A summary of the elastic moduli of PCL for different processing methods is

given in Table 1. β-TCP has good biocompatibility and osteoconductivity and has been used both on its own and in combination with polymers in scaffold applications[11,21,32,35,45,59].

PCL/ β-TCP scaffolds for bone tissue engineering applications similar to those used in this study have been fabricated with varying volume fractions[25,26,28,33,54]. An advantage of SLS is the high degree of repeatability and conformity of the scaffold to the original 3D CAD design on the macro-scale compared to the relatively random distribution of pores in scaffolds fabricated using, for example, salt leaching[8,27,48,61]. However, this type of scaffold material is inhomogeneous at the microscale level with the inclusion of micropores and β-TCP particles[33]. Previous studies have shown that simple 3D CAD geometries are insufficient to capture the mechanical behaviour of this type of SLS-fabricated scaffolds using finite element modelling[4,57]. By their nature, CAD models account for only the designed scaffold macroporosity and do not account for microporosity within the scaffold structure or surface roughness that are present due to the fabrication process. Cahill et al. found that models based on the designed scaffold geometry over-predicted the scaffold stiffness by up to 147% and that surface roughness is a factor that needs to be accounted for [4]. High resolution finite element meshes have been successfully generated from micro-CT scans giving accurate models of the real geometries of both bone tissue engineering scaffolds[6,10,38,49,50,52,57] and native bone tissue[2,29,40,47,51].

Micromechanics approaches to evaluate the mechanical properties of particle-reinforced composites traditionally use idealised microstructures based on particle distribution and are often modelled under periodic boundary conditions[5]. This approach was used by Eshragi et al. to determine the bulk mechanical properties of a PCL/hydroxyapatite SLS scaffold[14]. Methods such as this require assumptions and simplifications regarding microstructure geometry, particle distribution and particle size distribution. In the case where high resolution

images of the real material microstructure are available, effective properties for the material microstructure can be evaluated using uniform boundary conditions[20]. This approach has been applied to a range of applications including random heterogeneous materials[22], cancellous bone[43] and silicon carbide fibre reinforced composites[7]. The effective properties of particle reinforced composites have also been explored[15,23]; however the mechanical properties of this particular sintered material have not yet been explored using this method.

The primary aim of this study is to develop a method to accurately model the realistic mechanical behaviour of a sintered PCL/ β-TCP scaffold material. To achieve this, high-resolution finite element modelling of the material samples is used. A range of methods is then explored to determine the most appropriate and most practical way to assign the mechanical properties in the high resolution models, specifically the elastic constants. In particular, micromechanical modelling approaches are employed to determine appropriate elastic constants. Comparisons are made with the predictions of simpler approaches and recommendations are made on how best to determine elastic properties for such complex materials.

3 Methods

3.1 Materials & Fabrication

3.1.1 Materials

Poly-ε-caprolactone (PCL) powder (CAPA6506, Solvay, UK) with an average molecular weight (Mn) of 60,000 and a particle size of 600μm was cryogenically ground to a maximum particle size of 50μm. β-tricalcium phosphate (β-TCP) (Fluka) with a molecular weight of 310.18 g/mol and a particle size of 3-5μm was mixed with the PCL powder in a 50:50 wt% ratio (approximately 25 vol% β-TCP) using a hand mixer for five minutes until well blended.

3.1.2 Pure PCL tensile samples

Rectangular bars of pure PCL with rectangular cross section were fabricated using vacuum moulding for characterisation of the mechanical properties of PCL, with a specimen design based on type V of ASTM D638. A rectangular bar geometry was used as machining the material to a dog bone shape would have run the risk of exceeding the melt temperature of PCL. Stainless steel moulds with well dimensions 50 x 10 x 15mm were filled with 3g of PCL powder. The filled moulds were placed in an oven at 120°C under a vacuum for 5 hours to remove any air bubbles and allowed to cool. The solid samples were then removed from the moulds and cut to 3mm thickness to give a uniform cross-section of 3x10mm.

3.1.3 Single scaffold struts

Single bone tissue engineering scaffold struts were fabricated in ladders of 10 struts from the mixed PCL and β-TCP powders by SLS with the Sinterstation 2500^{plus} system (DTM, USA). These struts were designed to have the same dimensions as the individual scaffold struts in the PCL/TCP scaffolds used in Lohfeld et al.[34] and were manufactured using the same laser scan process as for struts in the scaffold. The dimensions of each individual strut are approximately 13mm length with an approximately rectangular cross section of 0.77mm x 0.55mm. In order to achieve this relatively small strut thickness in a scaffold with relatively small overall dimensions, the “outline scan” fabrication method described by Lohfeld et al. was employed[34]. A laser power of 7W was used, and the part bed heater was held at 49°C during fabrication. The build was paused for two minutes during heating up to 49°C to allow the powder to reach a uniform temperature prior to sintering. The nitrogen supply to the chamber was turned off, as it is not required for the materials being sintered. The powder layer thickness was set to 0.11mm. A total of 16 strut ladders were fabricated in a single fabrication run. An example of a strut ladder is shown in Figure 1a. Following the build, the

parts were left to cool in the machine part bed overnight and excess powder was removed using pressurised air.

3.2 Structural and Morphological Characterization

Prior to mechanical testing, high resolution scans of 40 single scaffold struts were obtained using a micro-computed tomography (μ-CT) scanner (SkyScan-1072 High-resolution desk-top micro-CT system, University of Aberdeen, UK) at a resolution of approximately 14.4μm. Higher resolution images of a small segment of a scaffold strut (approximate dimensions 0.77mm x 0.1mm x 0.1mm) were obtained using X-ray microtomography (XMT) (phoenix nanotom®, GE, at SEAM, Waterford Institute of Technology, Ireland) with a scan resolution of 1.2μm. Scaffolds were cut into 3mm thick sections using a backed blade, mounted on a coupon and gold-coated before imaging using a Hitachi S-4700 scanning electron microscope (SEM) (Hitachi, UK) at a power of 15kV. SEM images of the material microstructure are shown in Figure 1 b and c. The presence of both partially sintered and fully sintered regions of material are visible in Figure 1b, where partial sintering results in regions of porous material that will influence the overall mechanical behaviour of the scaffold material. The smaller β-TCP particles can be seen on the larger PCL particles in Figure 1c.

3.3 Mechanical characterisation

3.3.1 Pure PCL samples

Tensile tests were carried out on the pure PCL samples at room temperature using an Instron Series IX 4467 screw-driven testing system as per ISO 527-1, at a strain rate of 1% of the gauge length per minute. The initial gauge length was set to 20mm, with 15mm at each end held in the grips. The width (w) and thickness (t) of each sample were measured using a vernier callipers prior to testing and the original cross sectional area (CSA) was calculated as

CSA=w*t. The force (F) and change in gauge length were recorded. Uniaxial tensile engineering stress was calculated as per Equation 1 where A is the original CSA. The elastic modulus (E_{PCL}) was calculated as per Equation 2, where σ_a is the stress at ε_a and σ_b is the stress at ε_b, where ε is the tensile engineering strain and both ε_a and ε_b are taken in the initial linear region of the tensile curves for the material, in general accordance with ISO 527-1.

$$\sigma = \frac{F}{A} \quad (1)$$

$$E_{PCL} = \frac{\sigma}{\varepsilon} = \frac{\sigma_b - \sigma_a}{\varepsilon_b - \varepsilon_a} \quad (2)$$

3.3.2 Single struts

The mechanical properties of the individual scaffold struts were characterised through tensile testing. Compression testing would not have been practical due to a tendency towards buckling (as verified by some initial trials), a consequence of the sample geometry selected. Tensile test specimens were cut from the SLS PCL/β-TCP strut ladders (Figure 1a) using a blade. As the struts are porous and delicate with a relatively low stiffness, they could not be held directly in machine grips for tensile testing without permanently damaging the test sample when tightening the grips. In order to overcome this problem, they were glued to a stiffer material for testing using the process illustrated in Figure 2. Small plastic tubes with an outer diameter of 2.5mm and wall thickness of 0.4mm and a length of 10mm were used for this purpose. A cyanoacrylate adhesive (Loctite® Power Easy™) was then injected inside the tube using a syringe to fill the cavity (Figure 2). Conventional superglues are soaked up by the struts due to their porous nature whereas this glue has a higher viscosity which prevents this and also allows for easier manipulation of the samples. Each end of the strut was then carefully positioned with approximately 2mm of the strut length in contact with the glue inside the tube. This assembly was allowed to set for 3 hours before repeating to position

a tube on the remaining end of the strut. As alignment of the samples with the tensile axis during testing is critical, a plastic alignment guide consisting of a piece of thin plastic folded at an angle was used to align the tubes and the struts during the bonding process as shown in Figure 2. The full assembly was allowed to set overnight prior to mechanical testing. Uniaxial tensile tests were carried out at room temperature on a Zwick biaxial testing machine as per ISO 527-1, at a strain rate of 1% of the gauge length per minute. Strain was measured using a calibrated video extensometer camera. The average gauge length for samples tested was 6.994mm ± 0.766mm and dimensions were measured prior to testing using the calibrated video extensometer camera. Nominal strain and tensile elastic modulus were calculated as per ISO 527-1, as outlined above.

3.4 Finite element analysis

3.4.1 Full scaffold strut model

High resolution finite element (FE) models of the full scaffold struts were generated from micro-CT scans with a resolution of approximately 14.4μm. These images were manipulated to reduce the spatial resolution to an element length of 28.8μm to reduce the computational cost of running the models. The mesh module in the MIMICS software (Materialise, Belgium) was used to convert the micro-CT scan images to a high resolution FE mesh with 8-noded hexahedral voxel elements. Reduced integration was used for each strut model with the nonlinear geometry option selected. Meshes were generated for four individual struts, and tensile tests of each scaffold strut were simulated to replicate the experimental test set-up, as illustrated in Figure 3. The external nodes of the lower 2mm of the strut were fixed in the x, y, and z directions while an equation constraint was applied to the external nodes of the upper 2mm of the strut to constrain their movement in all directions to a controlling node. A tensile displacement of 1% of the gauge length was then applied to the controlling node. In order to

calculate strain in the gauge length in a comparable method to that used by the video extensometer software in the actual tensile tests, two nodes were selected at the same distance apart as the initial gauge length used by the video extensometer. Nominal strain was then measured by calculating the change in distance between these two nodes during the simulation and dividing by the original gauge length. Stress was calculated as the reaction force at the controlling node divided by the average cross-section area, and the effective strut modulus was calculated as per Section 3.2.1.

In all cases isotropic linear elastic constants were used. Three different methods for determining the elastic modulus were employed as described below. Abaqus/Standard V6.10 was used for the FE simulations, with the NLGEOM option selected to account for large deformations. Mesh sizes ranged between 196,541 and 216,103 elements.

3.4.1.1 PCL models

It was anticipated that the material properties of the PCL component would dominate the mechanical behaviour of the material as the SEM images indicated that it acts as a matrix to bind the materials together, as sintering is carried out above the melt temperature of PCL but below the melt temperature of β-TCP. Therefore, the first type of material assignment used was *homogeneous assignment* of isotropic linear elastic properties of PCL: $v = 0.3$ [13], and E_{PCL} determined from pure PCL tensile testing (Section 4.1.1). It should be noted that this method is not representative of the real material and is only intended as a comparison.

3.4.1.2 RoM models

In order to account for the presence of β-TCP in the sintered material the *rule of mixtures* (RoM) was used to calculate an effective modulus for the material as per Equation 3, where

E_X is the elastic modulus of material phase X, E_{RoM} is the modulus calculated using the rule of mixtures and vf_X is the volume fraction of each material phase X.

$$E_{RoM} = E_{PCL} vf_{pcl} + E_{TCP} vf_{TCP} \quad (3)$$

The elastic modulus of β-TCP was taken from Wang et al.[56] where the elastic modulus of sintered β-TCP was evaluated at different sintering temperatures. The average modulus at the lowest sintering temperature was chosen for this study, with a value of 24.6GPa.This gives a linear elastic composite modulus E_{RoM} = 277 x 0.75 + 24.6x10^3 x 0.25 = 6.36GPa; this was then assigned homogeneously to the strut geometries, with ν = 0.3 as before. The rule of mixtures applies specifically for the case of aligned fibre-reinforced composite, which is clearly different to the material configuration that we have here. However, as it is a well known well-known, straightforward method for determining the elastic moduli of composites it is used here for basic comparison purposes. Given that the rule of mixtures assumed configuration is of continuous fibres aligned in the loading direction, it is to be expected that it would over-predict the elastic modulus for the material presented here.

3.4.1.3 Microstructure-based models

In order to capture the local inhomogeneity of the sintered material and the contribution of the β-TCP particles to its mechanical performance, the effective elastic constants of segments of material equal in size to one element in the full strut models were incorporated from micromechanical modelling (described below in Section 3.3.2). Here, the micro-CT scan grey value of each element in the high resolution mesh is used to identify the appropriate values of effective isotropic elastic modulus (E_{eff}) and Poisson's ratio (ν_{eff}) to assign to this element using the relationship generated in the micromechanical analysis described in Section 3.3.2**,** as outlined in Figure 4. In order to implement this method, the material

expressions method in the MIMICS FEA module's material assignment tool was used to assign density, Young's Modulus and Poisson's ratio using Equations 4, 5 and 6 respectively, where a_1, a_2, a_3, b_1, b_2 and b_3 are user-defined constants, ρ is density, E is Young's Modulus and ν is Poisson's ratio. The constant a_1 and b_1 were set to one and zero respectively to make E and ν directly proportional to GV.

$$\rho = a_1 \times GV + b_1 \quad (4)$$

$$E = a_2 \times \rho + b_2 \quad (5)$$

$$\nu = a_3 \times \rho + b_3 \quad (6)$$

3.4.2 Micromechanical analysis

Due to the mixing of the powders prior to sintering and the difference in sizes of the PCL and β-TCP particles, there is an inhomogeneous distribution of materials in the resulting sintered material. In order to capture this inhomogeneity and to account for it in the generation of effective elastic constants for the material, FE models of cuboidal segments of material representing varying average grey-values were generated from the 1.2 µm XMT scan using MIMICS, as illustrated in Figure 4. Each segment has dimensions equal to one element in the full strut models (edge length 28.8µm). The thresholding and dynamic region growing tools in the MIMICS software package were used to isolate the PCL and β-TCP phases in the 1.2 µm XMT scan of the block of material. The average grey-value (GV_{ave}) was identified for each segment of material with 28.8µm edge length extracted from the XMT scan. A FE mesh with 8-noded hexahedral voxel elements with reduced integration was generated for each segment. The PCL and β-TCP phases were represented as separate sections in one meshed part and the appropriate linear elastic material properties were assigned to each phase. The experimentally evaluated elastic modulus for PCL ($E_{\mathbf{PCL}}$) of 277MPa, as per Section 4.1.1 below, was used for PCL phases and the elastic modulus of β-TCP was taken as 24.6GPa, as

per Section 3.3.1.2. A Poisson's ratio of 0.3 was assumed for both phases in all simulations and Abaqus/Standard V6.10 was used with NLGEOM selected.

Given that, in this particular implementation, material segment size has been fixed for the micromechanical model by the full strut model element size (edge length of 28.8μm), the "windowing approach" is used to generate the effective elastic constants (and specifically in this case an effective isotropic elastic modulus (E_{eff}) and Poisson's ratio (v_{eff})), as described for example in references[3,20,41]. Consistent with the windowing approach, three different sets of uniform boundary conditions were applied to the models as follows:

1. Kinematic uniform boundary conditions (KUBC): A macroscopically homogeneous strain tensor ε is imposed on all boundaries with radius vector x, giving a displacement vector ξ as per Equation 7, where ‹ε› is the volume averaged strain:

$$\boldsymbol{\xi} = \langle \boldsymbol{\varepsilon} \rangle * \boldsymbol{x} \tag{7}$$

2. Static uniform boundary conditions (SUBC): A macroscopically homogeneous stress tensor $\boldsymbol{\sigma}$ is imposed on all boundaries with exterior unit normal $\boldsymbol{n}$, giving a traction vector density $\boldsymbol{P}$ as per Equation 8, where $\langle \boldsymbol{\sigma} \rangle$ is the volume averaged stress:

$$\boldsymbol{P} = \langle \boldsymbol{\sigma} \rangle * \boldsymbol{n} \tag{8}$$

3. Mixed uniform boundary conditions (MUBC): These are a combination of the KUBC and SUBC as detailed in Appendix A.

For the first phase of model development, FE analyses of each segment under six modes of deformation were carried out under kinematic, static and mixed uniform boundary conditions in order to identify the effective isotropic elastic constants. Three tensile simulations in (1), (2) and (3) directions were simulated as well as three shear simulations in the (1-2), (2-3) and (3-1) planes. Details of the implementation of the three types of boundary conditions are outlined in Appendix A. The effective elastic constants (E_{eff} and v_{eff}) were determined for

each individual segment using strain energy density equivalence, as detailed in Appendix B. Segments with significant porosity were excluded due to the complications of assigning KUBC and SUBC to these segments. From consideration of the full data set of 100 28μm^3 segments generated from the XMT scan, the use of seven grey-value categories was judged to be sufficient to give a reasonable representation of the full data set. Seven levels of average grey-value were chosen within a range of 93 to 150 and meshes were generated to represent each level of grey-value, giving a total of 7 segments.

Results for the first phase of model development are given in Supplementary Figure S1, where E_{eff}, is plotted against grey-value for multiple segments with no porosity for each boundary condition case. The effective isotropic elastic modulus E_{eff} is plotted with respect to average grey-value for seven segment models covering a range of grey-values, representative of the spread of grey-values observed in the scans. From the results it can be noted that $E_{\text{eff}}^{\text{KUBC}} > E_{\text{eff}}^{\text{MUBC}} > E_{\text{eff}}^{\text{SUBC}}$, consistent with the expectations of the windowing approach on the effects of the different boundary condition types and the generation of upper and lower bounds to effective elastic modulus, as described in[3,20,41]. However it is observed that overall the differences between $E_{\text{eff}}^{\text{KUBC}}$ and $E_{\text{eff}}^{\text{SUBC}}$ are not that significant and indeed in one case $E_{\text{eff}}^{\text{KUBC}} \approx E_{\text{eff}}^{\text{MUBC}} \approx E_{\text{eff}}^{\text{SUBC}}$ indicating that a Representative Volume Element (RVE) has been identified [3].

The effective Poisson's ratio (ν_{eff}) results, as a function of GV_{ave}, are shown in Supplementary Figure S2. From these results it is evident that the differences in ν_{eff} are also not that large, consistent with the observation for E_{eff}; in fact, in all cases ν_{eff} was found to be very close to 0.3 with a mean value of 0.299 ± 0.17.

It is important to note that it would have been possible to generate effective anisotropic or orthotropic elastic constants for the material segments using the described modelling

framework; however the implementation of these material properties in the full strut models is impractical. This is because there is no directional dependence data available for the full strut models as they are generated from scan data and each element is described by only one number – its grey-value. Hence, an effective isotropic representation is the only practical option.

Based on the above, a second phase of model development was performed to generate the final set of effective isotropic elastic constants for the full strut model analyses. For these simulations, models of material segments that incorporate the presence of porosity were included to account for the possible presence of some micropores in the material that may not be captured in the full strut scan due to insufficient scan resolution. Neglecting the presence of these micropores could result in the models overestimating element stiffness.

Only MUBCs were applied to segments during this phase of modelling given the closeness of the $E_{\text{eff}}^{\text{KUBC}}$ and $E_{\text{eff}}^{\text{SUBC}}$ results from Supplementary Figure S1 and the fact that the $E_{\text{eff}}^{\text{MUBC}}$ results lie between these upper and lower bounds respectively. The MUBCs are also the simplest to assign to segments that include porosity. Seven levels of average grey-value were chosen within a range of 93 to 150, representative of the overall spread of grey-values observed in the material, and meshes were generated for three separate segments for each level to represent possible variations in material composition within each level of grey-value. Only two segments were successfully generated for the lowest range of grey-values as these segments typically had high levels of surface porosity making it difficult to assign boundary conditions, giving a total of 20 segments. The percentage of segment elements representing PCL, ß-TCP and pores for each segment as well as average segment grey-value are shown in Supplementary Figure S3. This plot shows that multiple different configurations of material

composition can exist with the same GV_{ave}. This can result in variation in E_{eff} and v_{eff} for one GV_{ave}, for example as represented by the data at GV_{ave} of 147 in Figure 7(a) and 8(a).

Each segment was modelled under the six modes of uniaxial and shear deformation with MUBC applied as per Appendix A. The equivalent isotropic elastic constants E_{eff} and v_{eff} were evaluated for each segment as per Appendix B. The average E_{eff} and v_{eff} for each grey-value level was calculated and is shown in Figure 7 (b) and Figure 8 (b) respectively; the line fit for each E_{eff} and v_{eff} was used to assign appropriate elastic constants in Section 3.4.1.3. As these are the final micromechanical models used in Section 3.4.1.3 above, results for this final phase of micromechanical modelling are presented in Section 4.2.1.

4 Results

4.1 Mechanical characterisation

4.1.1 Pure PCL samples

Tensile stress-strain curves for the pure PCL sample tests are shown in Figure 5. For the purposes of input into the finite element models, the elastic modulus is evaluated in the linear portion of the curve, i.e. up to a strain of 0.02. The linear elastic modulus of PCL is evaluated as 277.06 ± 27.66MPa (n=7), which is comparable to values observed in the literature listed in Table 1. This experimental value was used as input in the micromechanical simulations.

4.1.2 Single sintered struts

Single struts of composite sintered PCL and β-TCP were tested to failure in tension. Tensile stress-strain curves are shown in Figure 6 (a). The brittleness of the material relative to the pure PCL material, for example, should be noted. For comparison with the predictions of the elastic full strut finite element models the experimental effective strut elastic modulus was

determined from the initial linear elastic region (Figure 6 (b)), giving 98.87 ± 22.59MPa (n=7).

4.2 Finite element analysis

4.2.1 Micromechanical analysis

The results for the second phase of micromechanical modelling are shown in Figure 7 and Figure 8. As noted above, models for seven GV_{ave} values, with up to three segments per GV_{ave}, were used giving a total of 20 models. E_{eff} and ν_{eff}, are presented as a function of GV_{ave} in Figure 7 (a) and Figure 8 (a) respectively. The average E_{eff} and ν_{eff} for each for GV_{ave} was calculated and the linear relationship was determined as per Figure 7 (b) and Figure 8 (b) respectively giving the following relationships:

$$E_{\text{eff}} = m_E * GV_{ave} + c_E \quad (9)$$

$$\nu_{\text{eff}} = m_\nu * GV_{ave} + c_\nu \quad (10)$$

Here m_x and c_x are the slope and constant of the line describing the linear relationship between the constant x and average segment grey-value for Equations 9 and 10 above, and are given in Figure 7 (b) and Figure 8 (b) respectively. E_{eff} ranged from 277.43MPa to 374.45MPa with a mean value of 324.69MPa, and Poisson's ratio varied from 0.2393 to 0.3517 with a mean value of 0.289. The relationships described by Equations 9 and 10 above were used to assign element specific effective elastic constants (E_{eff} and ν_{eff}) in the full strut models as a function of average segment grey-value.

4.2.2 Macro-scale analysis of struts

The effective strut modulus was determined from the full strut models for each material assignment case described in Section 3.3.1: PCL, RoM and Microstructure-based. These values are shown in comparison with the experimentally evaluated strut modulus in Figure 9. Strut models utilising E_{PCL} (n = 4) gave an effective strut modulus with no statistical

difference from the experimentally observed strut modulus (n = 7) when compared using a Mann-Whitney test (p-value = 0.0726). A non-parametric test was used due to low sample numbers. Models using E_{RoM} aim to account for the contribution of the β-TCP particles present in the material to the overall strut mechanical performance by using the rule of mixtures to calculate a composite modulus including both PCL and β-TCP phase, but this method actually overestimates the experimentally observed strut stiffness by a factor of 27.

Analysis of the results show no statistical difference between the experimental strut modulus (n = 7) and the effective strut modulus evaluated using E_{eff} and v_{eff} (n = 4) when compared using a Mann-Whitney test (p-value = 0.0726). A non-parametric test was used due to low sample numbers. This indicates that using E_{eff} and v_{eff} gives a better approximation of the mechanical behaviour of the sintered PCL/ β-TCP strutsthan other material assignment methods that accounted for the presence of both PCL and β-TCP.

In addition, other versions of the microstructure-based models were formulated for comparison purposes, and results for these models are compared included in Figure 9, namely:

- Element-specific assignment of elastic modulus using E_{eff} as per 3.3.1.3, but using a constant Poisson's ratio of 0.3, labelled as $E_{eff}^{0.3}$ in Figure 9.
- Homogeneous assignment of elastic constants, using the minimum value of grey-value averaged E_{eff} of 277.43MPa and a constant Poisson's ratio of 0.3, labelled as E_{eff}^{MIN} in Figure 9.
- Homogeneous assignment of elastic constants, using the mean value of grey-value averaged E_{eff} of 324.69MPa and a constant Poisson's ratio of 0.3, labelled as E_{eff}^{MEAN} in Figure 9.

- Homogeneous assignment of elastic constants, using the maximum value of grey-value averaged E_{eff} of 374.45MPa and a constant Poisson's ratio of 0.3, labelled as E_{eff}^{MAX} in Figure 9.

As it is evident from the figure, keeping the Poisson's ratio constant at 0.3 ($E_{eff}^{0.3}$ case) has a negligible effect on overall modulus prediction, whereas using a homogeneous minimum or maximum value for elastic modulus does have a noticeable effect (E_{eff}^{MIN} and E_{eff}^{MAX} cases).

5 Discussion

The linear elastic properties of solid PCL tensile samples fabricated by vacuum melting were evaluated giving an elastic modulus of 277.06 ± 27.66MPa. This falls within the expected range when compared to the literature in Table 1[9,13,14,31,39,42,46,53,57]. The linear elastic properties of single sintered PCL/ β-TCP struts fabricated by SLS were evaluated giving an average elastic modulus of 98.87 ± 22.59MPa. Comparison of elastic moduli of the pure PCL samples and sintered struts reveals that the pure PCL samples are approximately three times stiffer than the sintered struts, despite the inclusion of β-TCP particles that are 88.8 times stiffer than PCL. The reason for this difference is the presence of pores in the sintered struts, whereas the pure PCL samples have no porosity. Other studies where PCL-based composites were fabricated with the inclusion of particles such as TCP[25], phosphate glass[53] and TiO_2[18] have shown an initial increase in stiffness, however in these cases there was no increase in porosity as a result of the addition of the particles. These studies also found that the rate of degradation was affected by the addition of the particles, which should be taken into consideration in studies involving the change in material properties over time, but was not the focus of the present study.

In the SEM images of the scaffold struts, fully sintered areas are visible as smooth surfaces in Figure 1b, and partially-sintered areas are also visible. These images indicate that the material has a porous microstructure, resulting in lower mechanical properties than the solid PCL samples. Examination of the XMT scans indicates that the β-TCP particles are embedded in a PCL matrix (Figure 1b), therefore the mechanical behaviour of the sintered material may be dominated by the stiffness of the PCL phase. This was approximated in full strut models using E_{PCL}, where homogeneous PCL properties were assigned. These models were found to give a good estimate of strut effective modulus when compared to the experimental results, however they are not sufficiently representative of the real material as it does not account for both PCL and β-TCP phases. The primary purpose of the addition of ß-TCP particles to this material is to promote osteogenesis, i.e. the formation of new bone, and not necessarily to change mechanical properties. FE models with homogeneous PCL properties assigned to PCL/β-TCP strut geometries were included here for comparison purposes only.

Full strut models using E_{RoM} aim to account for the influence of β-TCP particles on strut stiffness using a homogeneous elastic modulus calculated based on the volume fractions of PCL and β-TCP in the material. The strut elastic moduli for simulations using E_{RoM} overestimated the experimentally observed strut stiffness by a factor of 27 indicating that this method of material assignment is overly simplistic when dealing with a material with a complex microstructure such as this. As discussed in Section 3.4.1.2, it is to be expected that it would over-predict the elastic modulus of this material as the rule of mixtures assumed configuration is of continuous fibres aligned in the loading direction.

The XMT scans reveal that strut microstructure is inhomogeneous by nature and may play a role in the mechanical behaviour of the sintered material. Micromechanical modelling methods were successfully employed to calculate effective isotropic constants E_{eff} and ν_{eff} for

material segments. It was found that E_{eff} increases linearly with increasing grey-value, which is expected as the grey-value of the stiffer β-TCP particles is greater than the grey-value of the softer PCL regions. This means that increasing grey-value indicates increasing β-TCP content, resulting in increased stiffness. Consideration Figure 7 (b) and Figure 8 (b) would appear to indicate that E_{eff} and ν_{eff} are not hugely sensitive to changes in average grey-value over the range considered. E_{eff} has an increase of only 97.02MPa (35%) over an increase of 54.38 (57%) in grey-value, while ν_{eff} increases from 0.2393 to 0.3517 over a 57% increase in grey-value. For example the maximum value of E_{eff} is still far lower than that estimated by the rule of mixtures (E_{RoM}).

The relationships between the elastic constants and average grey-value were then used to assign element-specific effective elastic properties to the full strut meshes to determine strut effective stiffness. The use of E_{eff} and ν_{eff} was found to be the most accurate method of assigning elastic constants explored here with no statistical difference between the experimental strut modulus and the computational strut modulus. This method of using micromechanical models to inform the appropriate local mechanical properties in the full strut model gives improved accuracy in modelling this type of SLS fabricated scaffold material in comparison to other methods explored here as these were either not representative of the real sintered material or significantly overestimated the strut stiffness. Using E_{eff} and ν_{eff} gives a method of incorporating the β-TCP phase in the material while giving an accurate representation of the real mechanical behaviour of the sintered material.

We also compared the results of our simulations using E_{eff} and ν_{eff} to simulations using homogeneous assignment of E_{eff}^{MIN}, E_{eff}^{MAX} and E_{eff}^{MEAN} and $\nu = 0.3$ in Figure 9. The closest estimate of the experimentally observed strut effective modulus is given by E_{eff}^{MIN} while both E_{eff}^{MEAN} and E_{eff}^{MAX} give less accurate estimations of strut stiffness with higher values than

strut stiffness evaluated using E_{eff} and ν_{eff}. If grey-value throughout the strut was uniform and equal to the mean value of the grey-value range considered here (mean of range 93 to 150), it would be safe to assume that the best approximation of the experimental modulus would be given by E_{eff}^{MEAN}. This is not the case here and the strut modulus generated using E_{eff} is in fact closest in value to that generated using a homogenous assignment of E_{eff}^{MIN}, indicating that the majority of elements in the strut have a grey-value at the lower end of the range of grey-values. The situation might be quite different if for example the distribution of grey-values in the strut models was predominantly towards the higher end of the range; in this case a homogeneous assignment of E_{eff}^{MAX} might be closest to E_{eff} in terms of strut modulus prediction. The implication is that it would not be sufficiently accurate to take a simple approach and assume that one can use a homogeneous E_{eff}^{MEAN} to accurately predict strut modulus, even though as observed above the dependence of E_{eff} on GV_{ave} does not appear to be particularly strong. On the contrary, the indications are that an element-specific elastic property (E_{eff} and ν_{eff}) assignment by average grey-value is required for accuracy.

To explore this further, simulations were also carried out using a constant Poisson's ratio of 0.3 and an element-specific E_{eff}, $E_{eff}^{0.3}$, see Figure 9, giving an almost identical strut effective modulus to that of E_{eff} and ν_{eff} when compared using an unpaired t-test (P = 0.9479, n = 4) with no statistical difference from the experimentally observed modulus (P = 0.0555). This means that for the prediction of strut stiffness the variation of elastic modulus with grey-value is more significant than the variation of Poisson's ratio with grey-value. In fact, this result may indicate that it is acceptable to assume a homogeneous Poisson's ratio in this type of analysis, however this may just be the case for this material and the validity of using a constant Poisson's ratio should be determined for the specific material being studied. In relation to the potential acceptability of using a homogeneous Poisson's ratio, the same cannot be said for elastic modulus; even though the dependence of E_{eff} on GV_{ave} may not be

that strong (Figure 7 (b)), the variation is sufficient to generate a noticeable effect at the macroscale (full strut model stiffness), as represented by the $E_{\text{eff}}^{\text{MIN}}$, $E_{\text{eff}}^{\text{MAX}}$ and $E_{\text{eff}}^{\text{MEAN}}$ cases in Figure 9.

The micromechanical modelling implementation reported here is specific to the constituent material properties and the ratio of powder blend used. In order to be accurate for different powder blends, micromechanical analysis of the specific sintered material is required to identify the relationship between grey-value and elastic constants specific to that material. The direction of sintering may also influence the accuracy of this method, as previous studies have shown that the density and overall mechanical properties of solid sintered parts can vary with orientation of the sintered part in the part bed, i.e. whether the part oriented is parallel or perpendicular to the laser path[13]. However, this variation is presumably due to variations in local densities in the directions parallel or perpendicular to the laser path and density is directly related to grey-value. As E_{eff} and ν_{eff} are controlled by grey-value, it is expected that this method would be sensitive enough to capture these differences provided that sufficient mesh resolution is obtained to capture local variations in density.

As discussed above, the resulting geometries of selective laser sintered products, as used in this study, are not the same as the idealised CAD geometries from which they were designed. Idealised microstructures were used in FE modelling of idealised sintered PCL/Hydroxyapatite scaffold geometries to predict the effect of varying percentages of HA on scaffold stiffness by Eshraghi et al[14]. The lack of realistic geometries and microstructures in their study may account for some of the discrepancies between computational and experimental results. Our study is based on similar principles, but includes high resolution FE meshes to account for the real geometry of the sintered materials and incorporates micromechanical models developed using real as opposed to idealised microstructure

geometries to capture the real geometries on both the macro- and micro-scale as accurately as possible. Harrison et al. included the influence of locally-varying mechanical properties on macroscale mechanical behaviour of trabecular bone by using voxel-specific mechanical properties determined using nanoindentation[19]. In a similar approach, Scheiner et al. used the Mori-Tanaka scheme to generate and assign homogenised voxel-specific properties based on grey-value to include the influence of material microstructure on the mechanical performance of glass-ceramic scaffolds and found good correlation between computational results and ultrasonic measurements[52]. We have also incorporated voxel- or element-specific assignment of material properties in order to account for variations in local mechanical properties due to variations in material distributions. However, we have generated effective material properties from microstructural models specific to the real geometry of the material microstructure to account for the highly heterogeneous and complex nature of the microstructure of this sintered material. By including both real micro- and macro-scale geometries and locally-varying mechanical properties, we have developed a method capable of accounting for the influence of both the influence of microstructural geometries and stiffness on the macroscale behaviour of these sintered PCL/ β-TCP scaffold materials. An advantage of the method that we have developed here is that information about local stiffness at the level of cells seeded on a scaffold is retained through element-specific assignment of material properties. This has significance as it has been shown that local stiffness influences tissue differentiation[12]; in particular, regions of high material stiffness can act as nucleation sites for mineralisation and new bone formation[1]. Using the methods presented here, information about local stiffness could, in theory, be used to direct tissue differentiation in studies looking at tissue formation in a scaffold-filled defect.

In this study, we have demonstrated that our modelling methods can accurately predict the macroscale mechanical behaviour of SLS scaffold material when compared with the results

of tensile tests on the actual material. This has been achieved by attempting to accurately capture the microscale architecture and composition of the material in micromechanical models. Given that these models have now been generated and have been validated by their accurate prediction of experimentally measured (macroscale) mechanical behaviour, the use of these models for other purposes relevant to tissue engineering scaffold mechanics can be considered. Chief among these is the characterisation and quantification of the microscale strain and stress state in the material and at the pore surfaces, to get a direct understanding of the micro-biomechanical stimuli that cells will experience when seeded in the scaffold. This has significant implications for scaffold design and is the subject of on-going investigation by the authors.

6 Conclusion

This paper presents a novel method to improve the ability of FE models to capture the real mechanical behaviour of selective laser sintered materials. The traditional rule of mixtures method for modelling composite materials was shown to be inaccurate for this type of material as it significantly overestimated the strut modulus. The use of solid PCL properties gave a good estimate of strut modulus; however it is not representative of the real material as it does not account for the presence of the β-TCP phase in the material. Micromechanical modelling methods were used to determine a relationship between grey-value and effective isotropic elastic constants for segments of material equal in size to one element in the full strut models. There was no statistical difference between the experimentally evaluated strut modulus and a computationally evaluated modulus from simulations using element-specific elastic constants assigned based on grey-value. These results indicate that incorporating micro-scale mechanical analysis of the sintered scaffold material in macroscale FE modelling

of sintered structures gives an accurate prediction the mechanical behaviour of these sintered structures.

7 Acknowledgements

H.Doyle acknowledges funding from the Irish Research Council under the Embark Initiative Postgraduate Research Scholarship Scheme. The authors would like to acknowledge the SFI/HEA funded Irish Centre for High End Computing for the provision of computational resources and support. The authors would also like to acknowledge input from Jamie Madden and Alberto Alvarez of the Mathematics Department at NUI Galway.

8 References

1. Bhumiratana, S., W. L. Grayson, A. Castaneda, D. N. Rockwood, E. S. Gil, D. L. Kaplan, and G. Vunjak-Novakovic. Nucleation and growth of mineralized bone matrix on silk-hydroxyapatite composite scaffolds. *Biomaterials* 32:2812–20, 2011.

2. Bitsakos, C., J. Kerner, I. Fisher, and A. a Amis. The effect of muscle loading on the simulation of bone remodelling in the proximal femur. *Journal of Biomechanics* 38:133–9, 2005.

3. Bohm, H. J. A Short Introduction to Continuum Micromechanics. In: Mechanics of Microstructured Materials, edited by H. J. Bohm. Vienna: CISM Courses and Lectures, Springer-Verlag, 2004, pp. 1–40.

4. Cahill, S., S. Lohfeld, and P. E. McHugh. Finite element predictions compared to experimental results for the effective modulus of bone tissue engineering scaffolds fabricated by selective laser sintering. *Journal of Materials Science. Materials in Medicine* 20:1255–62, 2009.

5. Chan, K. S., W. Liang, W. L. Francis, and D. P. Nicolella. A multiscale modeling approach to scaffold design and property prediction. *Journal of the Mechanical Behavior of Biomedical Materials* 3:584–93, 2010.

6. Charles-Harris, M., S. del Valle, E. Hentges, P. Bleuet, D. Lacroix, and J. a Planell. Mechanical and structural characterisation of completely degradable polylactic acid/calcium phosphate glass scaffolds. *Biomaterials* 28:4429–38, 2007.

7. Chateau, C. Multiscale approach of mechanical behaviour of SiC / SiC composites : elastic behaviour at the scale of the tow. *Technische Mechanik* 30:45–55, 2010.

8. Chatterjee, K., L. Sun, L. C. Chow, M. F. Young, and C. G. Simon. Combinatorial screening of osteoblast response to 3D calcium phosphate/poly(ε-caprolactone) scaffolds using gradients and arrays. *Biomaterials* 32:1361–1369, 2010.

9. Chen, B., K. Sun, and T. Ren. Mechanical and viscoelastic properties of chitin fiber reinforced poly(ε-caprolactone). *European Polymer Journal* 41:453–457, 2005.

10. Van Cleynenbreugel, T., J. Schrooten, H. Van Oosterwyck, and J. Vander Sloten. Micro-CT-based screening of biomechanical and structural properties of bone tissue engineering scaffolds. *Medical & Biological Engineering & Computing* 44:517–25, 2006.

11. Dong, J., T. Uemura, Y. Shirasaki, and T. Tateishi. Promotion of bone formation using highly pure porous beta-TCP combined with bone marrow-derived osteoprogenitor cells. *Biomaterials* 23:4493–502, 2002.

12. Engler, A. J., S. Sen, H. L. Sweeney, and D. E. Discher. Matrix elasticity directs stem cell lineage specification. *Cell* 126:677–89, 2006.

13. Eshraghi, S., and S. Das. Mechanical and microstructural properties of polycaprolactone scaffolds with one-dimensional, two-dimensional, and three-dimensional orthogonally oriented porous architectures produced by selective laser sintering. *Acta Biomaterialia* 6:2467–76, 2010.

14. Eshraghi, S., and S. Das. Micromechanical finite-element modeling and experimental characterization of the compressive mechanical properties of polycaprolactone-hydroxyapatite composite scaffolds prepared by selective laser sintering for bone tissue engineering. *Acta Biomaterialia* , 2012.doi:10.1016/j.actbio.2012.04.022

15. Galli, M., and J. Botsis. An Elastoplastic Three Dimensional Homogenization Model for Particle Reinforced Composites. *Computational Materials Science* 41:312–321, 2008.

16. Guldberg, R. E., N. J. Caldwell, X. E. Guo, R. W. Goulet, S. J. Hollister, and S. a Goldstein. Mechanical stimulation of tissue repair in the hydraulic bone chamber. *Journal of Bone and Mineral Research : the Official Journal of the American Society for Bone and Mineral Research* 12:1295–302, 1997.

17. Gunatillake, P. a, and R. Adhikari. Biodegradable synthetic polymers for tissue engineering. *European Cells & Materials* 5:1–16, 2003.

18. Gupta, K. K., A. Kundan, P. K. Mishra, P. Sirvastava, S. Mohanty, N. K. Singh, A. Mishra, and P. Maiti. Polycaprolactone composites with TiO 2 for potential nanobiomaterials: tunable properties using different phases. *Phys. Chem. Chem. Phys.* 14:12844–12853, 2012.

19. Harrison, N. M., P. F. McDonnell, D. C. O'Mahoney, O. D. Kennedy, F. J. O'Brien, and P. E. McHugh. Heterogeneous linear elastic trabecular bone modelling using micro-CT attenuation data and experimentally measured heterogeneous tissue properties. *Journal of Biomechanics* 41:2589–96, 2008.

20. Hazanov, S. Hill condition and overall properties of composites. *Archive of Applied Mechanics* 68:385–394, 1998.

21. Kang, Y., A. Scully, D. a Young, S. Kim, H. Tsao, M. Sen, and Y. Yang. Enhanced mechanical performance and biological evaluation of a PLGA coated β-TCP composite scaffold for load-bearing applications. *European Polymer Journal* 47:1569–1577, 2011.

22. Kanit, T., and S. Forest. Determination of the size of the representative volume element for random composites : statistical and numerical approach. *International Journal of Solids and Structures* 40:3647–3679, 2003.

23. Kanit, T., F. N'Guyen, S. Forest, D. Jeulin, M. Reed, and S. Singleton. Apparent and effective physical properties of heterogeneous materials: Representativity of samples

of two materials from food industry. *Computer Methods in Applied Mechanics and Engineering* 195:3960–3982, 2006.

24. Koike, M., H. Shimokawa, Z. Kanno, K. Ohya, and K. Soma. Effects of mechanical strain on proliferation and differentiation of bone marrow stromal cell line ST2. *Journal of Bone and Mineral Metabolism* 23:219–25, 2005.

25. Lam, C. X. F., M. M. Savalani, S.-H. Teoh, and D. W. Hutmacher. Dynamics of in vitro polymer degradation of polycaprolactone-based scaffolds: accelerated versus simulated physiological conditions. *Biomedical Materials* 3:034108, 2008.

26. Lee, H., and G. Kim. Three-dimensional plotted PCL/β-TCP scaffolds coated with a collagen layer: preparation, physical properties and in vitro evaluation for bone tissue regeneration. *Journal of Materials Chemistry* 21:6305, 2011.

27. Lee, S. J., G. J. Lim, J.-W. Lee, A. Atala, and J. J. Yoo. In vitro evaluation of a poly(lactide-co-glycolide)-collagen composite scaffold for bone regeneration. *Biomaterials* 27:3466–72, 2006.

28. Lei, Y., B. Rai, K. Ho, and S. Teoh. In vitro degradation of novel bioactive polycaprolactone—20% tricalcium phosphate composite scaffolds for bone engineering. *Materials Science and Engineering: C* 27:293–298, 2007.

29. Liebschner, M. a K., R. Müller, S. J. Wimalawansa, C. S. Rajapakse, and G. H. Gunaratne. Testing two predictions for fracture load using computer models of trabecular bone. *Biophysical Journal* 89:759–67, 2005.

30. Liedert, A., D. Kaspar, R. Blakytny, L. Claes, and A. Ignatius. Signal transduction pathways involved in mechanotransduction in bone cells. *Biochemical and Biophysical Research Communications* 349:1–5, 2006.

31. Little, U., F. Buchanan, E. Harkin-Jones, M. McCaigue, D. Farrar, and G. Dickson. Accelerated degradation behaviour of poly(ε-caprolactone) via melt blending with poly(aspartic acid-co-lactide) (PAL). *Polymer Degradation and Stability* 94:213–220, 2009.

32. Liu, G., L. Zhao, L. Cui, W. Liu, and Y. Cao. Tissue-engineered bone formation using human bone marrow stromal cells and novel beta-tricalcium phosphate. *Biomedical Materials* 2:78–86, 2007.

33. Lohfeld, S., S. Cahill, V. Barron, P. McHugh, L. Dürselen, L. Kreja, C. Bausewein, and A. Ignatius. Fabrication, mechanical and in vivo performance of polycaprolactone/tricalciumphosphate composite scaffolds. *Acta Biomaterialia* 8:3446–3456, 2012.

34. Lohfeld, S., M. A. Tyndyk, S. Cahill, N. Flaherty, V. Barron, and P. E. McHugh. A method to fabricate small features on scaffolds for tissue engineering via selective laser sintering. *Journal of Biomedical Science and Engineering* 03:138–147, 2010.

35. Lu, Z., and H. Zreiqat. Beta-tricalcium phosphate exerts osteoconductivity through alpha2beta1 integrin and down-stream MAPK/ERK signaling pathway. *Biochemical and Biophysical Research Communications* 394:323–9, 2010.

36. Melchels, F. P. W., B. Tonnarelli, A. L. Olivares, I. Martin, D. Lacroix, J. Feijen, D. J. Wendt, and D. W. Grijpma. The influence of the scaffold design on the distribution of adhering cells after perfusion cell seeding. *Biomaterials* 32:2878–2884, 2011.

37. Middleton, J. C., and a J. Tipton. Synthetic biodegradable polymers as orthopedic devices. *Biomaterials* 21:2335–46, 2000.

38. Milan, J.-L., J. a Planell, and D. Lacroix. Simulation of bone tissue formation within a porous scaffold under dynamic compression. *Biomechanics and Modeling in Mechanobiology* 9:583–96, 2010.

39. Mondrinos, M. J., R. Dembzynski, L. Lu, V. K. C. Byrapogu, D. M. Wootton, P. I. Lelkes, and J. Zhou. Porogen-based solid freeform fabrication of polycaprolactone – calcium phosphate scaffolds for tissue engineering. *Biomaterials* 27:4399–4408, 2006.

40. Nawathe, S., F. Juillard, and T. M. Keaveny. Theoretical bounds for the influence of tissue-level ductility on the apparent-level strength of human trabecular bone. *Journal of Biomechanics* 46:1293–9, 2013.

41. Nemat-Nasser, S., and M. Hori. Micromechanics: Overall Properties of Heterogeneous Materials. *Elsevier* 687, 1993.

42. Ng, C. S., S. H. Teoh, T. S. Chung, and D. W. Hutmacher. Simultaneous biaxial drawing of poly (e-caprolactone) films. *Polymer* 41:5855–5864, 2000.

43. Pahr, D. H., and P. K. Zysset. Influence of boundary conditions on computed apparent elastic properties of cancellous bone. *Biomechanics and Modeling in Mechanobiology* 7:463–476, 2008.

44. Di Palma, F., A. Guignandon, A. Chamson, M.-H. Lafage-Proust, N. Laroche, S. Peyroche, L. Vico, and A. Rattner. Modulation of the responses of human osteoblast-like cells to physiologic mechanical strains by biomaterial surfaces. *Biomaterials* 26:4249–57, 2005.

45. Rai, B., J. L. Lin, Z. X. H. Lim, R. E. Guldberg, D. W. Hutmacher, and S. M. Cool. Differences between in vitro viability and differentiation and in vivo bone-forming efficacy of human mesenchymal stem cells cultured on PCL-TCP scaffolds. *Biomaterials* 31:7960–70, 2010.

46. Roosa, S. M. M., J. M. Kemppainen, E. N. Moffitt, P. H. Krebsbach, and S. J. Hollister. The pore size of polycaprolactone scaffolds has limited influence on bone regeneration in an in vivo model. *Journal of Biomedical Materials Research Part A* 92:359–68, 2010.

47. Roshan-Ghias, A., F. M. Lambers, M. Gholam-Rezaee, R. Müller, and D. P. Pioletti. In vivo loading increases mechanical properties of scaffold by affecting bone formation and bone resorption rates. *Bone* 49:1357–64, 2011.

48. Sabir, M. I., X. Xu, and L. Li. A review on biodegradable polymeric materials for bone tissue engineering applications. *Journal of Materials Science* 44:5713–5724, 2009.

49. Saey, H., and D. W. Hutmacher. Application of micro CT and computation modeling in bone tissue engineering. *Computer-Aided Design* 37:1151–1161, 2005.

50. Sandino, C., and D. Lacroix. A dynamical study of the mechanical stimuli and tissue differentiation within a CaP scaffold based on micro-CT finite element models. *Biomechanics and Modeling in Mechanobiology* , 2010.doi:10.1007/s10237-010-0256-0

51. Sanyal, A., A. Gupta, H. H. Bayraktar, R. Y. Kwon, and T. M. Keaveny. Shear strength behavior of human trabecular bone. *Journal of Biomechanics* 45:2513–9, 2012.

52. Scheiner, S., R. Sinibaldi, B. Pichler, V. Komlev, C. Renghini, C. Vitale-Brovarone, F. Rustichelli, and C. Hellmich. Micromechanics of bone tissue-engineering scaffolds, based on resolution error-cleared computer tomography. *Biomaterials* 30:2411–9, 2009.

53. Shah, M., I. Ahmed, B. Marelli, C. Rudd, M. N. Bureau, and S. N. Nazhat. Acta Biomaterialia Modulation of polycaprolactone composite properties through incorporation of mixed phosphate glass formulations. *Acta Biomaterialia* 6:3157–3168, 2010.

54. Shao, X., J. C. H. Goh, D. W. Hutmacher, E. H. Lee, and G. Zigang. Repair of large articular osteochondral defects using hybrid scaffolds and bone marrow-derived mesenchymal stem cells in a rabbit model. *Tissue Engineering* 12:1539–51, 2006.

55. Vance, J., S. Galley, D. F. Liu, and S. W. Donahue. Mechanical stimulation of MC3T3 osteoblastic cells in a bone tissue-engineering bioreactor enhances prostaglandin E2 release. *Tissue Engineering* 11:1832–9, 2005.

56. Wang, C., X. Zhou, and M. Wang. Influence of sintering temperatures on hardness and Young's modulus of tricalcium phosphate bioceramic by nanoindentation technique. *Materials Characterization* 52:301–307, 2004.

57. Williams, J. M., A. Adewunmi, R. M. Schek, C. L. Flanagan, P. H. Krebsbach, S. E. Feinberg, S. J. Hollister, and S. Das. Bone tissue engineering using polycaprolactone scaffolds fabricated via selective laser sintering. *Biomaterials* 26:4817–27, 2005.

58. Willie, B. M., D. Ph, X. Yang, N. H. Kelly, J. Han, T. Nair, T. M. Wright, M. C. H. Van Der Meulen, and M. P. G. Bostrom. Cancellous Bone Osseointegration Is Enhanced by In Vivo Loading. *Bone* 16:, 2010.

59. Wongwitwichot, P., J. Kaewsrichan, K. H. Chua, and B. H. I. Ruszymah. Comparison of TCP and TCP/HA Hybrid Scaffolds for Osteoconductive Activity. *The Open Biomedical Engineering Journal* 4:279–85, 2010.

60. Woodruff, M. A., and D. W. Hutmacher. The return of a forgotten polymer—Polycaprolactone in the 21st century. *Progress in Polymer Science* 35:1217–1256, 2010.

61. Wu, F., C. Liu, B. O'Neill, J. Wei, and Y. Ngothai. Fabrication and properties of porous scaffold of magnesium phosphate/polycaprolactone biocomposite for bone tissue engineering. *Applied Surface Science* 258:7589–7595, 2012.

9 Table and Figure Captions

Table 1: Literature survey of mechanical properties of PCL[9, 13, 14, 31, 39, 42, 46, 53, 57].

Table A.1: This table summarises the boundary conditions used for the assignment of kinematic, static and mixed uniform boundary conditions. Here, ε_{11} is strain in the positive x-direction, σ_{11} is stress in the positive x-direction, ε is the magnitude of the applied strain, and σ is the magnitude of the applied stress.

Figure 1: Selective laser sintered strut ladder (a).SEM images of the PCL/β-TCP scaffolds showing areas of fully sintered material (*) and partially sintered material (**) (b). A higher magnification image (c) shows β-TCP (*) and PCL (**).

Figure 2: Preparation of tensile test specimens from single struts.

Figure 3: Schematic diagram of tensile test set-up for single strut testing (left) and finite element model set-up for tensile test simulation (right).

Figure 4: Micromechanical models are used to generate E_{eff} data, which is then used to assign individual specific element mechanical properties based on average element grey-value.

Figure 5: Tensile curves for pure PCL samples tested to 0.2 strain.

Figure 6: Tensile curves for sintered struts tested to failure, with n=7 (a). Expanded view of the linear region of tensile curves for evaluation of elastic modulus (b).

Figure 7: Variation of E_{eff} with average grey-value with multiple segments for each grey-value (a) and variation of grey-value averaged E_{eff} with average grey-value (b), both for the second phase of model development.

Figure 8: Variation of Poisson's ratio (ν_{eff}) with average segment grey-value with multiple segments for each grey-value (a) and variation of grey-value averaged ν_{eff} with average segment grey-value, both for the second phase of model development.

Figure 9: Comparison of experimental (red, n = 7) and computationally evaluated (blue, n = 4) strut effective moduli for different methods of material assignment, with input material property type indicated on the x-axis. E_{eff} uses heterogeneous assignment of E_{eff} and ν_{eff}, while $E_{eff}^{0.3}$ uses heterogeneous assignment of E_{eff} and a constant Poisson's ratio of 0.3. E_{eff}^{MIN}, E_{eff}^{MEAN} and E_{eff}^{MAX} use homogeneous assignment of the minimum, mean and maximum values of E_{eff} respectively, each with a constant Poisson's ratio of 0.3. E_{PCL} and E_{RoM} use homogeneous assignment of the elastic modulus of PCL and a composite modulus calculated using the RoM respectively, with a constant Poisson's ratio of 0.3. Note that the plot is shown with a broken y-axis in order to show the RoM result on the same plot as the experimental results.

Figure A.1: Notation used to describe the faces of a cube segment for the application of uniform boundary conditions discussed in Appendix A.

Figure S1: E_{eff} plotted against average segment grey-value for segments in the first phase of model development.

Figure S2: Poisson's ratio ν_{eff} plotted against average segment grey-value for segments in the first phase of model development.

Figure S3: Segment material composition and average segment grey-value for segments in the second phase of model development.

Appendix A

1 Implementation of Boundary Conditions

This appendix outlines the implementation of the three types of boundary conditions used in the simulation of the microstructure segment models. Figure A.1 outlines the notation used to describe the faces of a segment cube for this appendix, and full details of the boundary conditions prescribed are given in Table A.1.

1.1 Kinematic uniform boundary conditions

Kinematic boundary conditions (KUBC) are implemented by assigning boundary conditions such that the average strains in all directions other than the loading direction must be equal to zero. For the case of uniaxial strain in the x-direction, a strain is applied on the positive x-face (F_{X1}) and the strain on all other faces is constrained perpendicular to the plane of each face, meaning that the strains on theses faces are equal to zero while the stresses are not equal to zero. In each loading case, the corners of the cube were constrained such that rotations about the x, y and z axes were prevented.

For the case of simple shear with KUBC, *EQUATION constraints were used within Abaqus to keep the faces straight by specifying the displacement of each node on the face. For the case of simple shear in the 1-2 direction, the equation for the displacement of a node on face F_{X1} is as per Equation A.1:

$$dx_{NODE} = dx_{CN} * (Y_{NODE}/Y_{SEG}) \quad \text{(A.1)}$$

Where dx_{NODE} is the nodal displacement in the x-direction, dx_{CN} is the nodal displacement in the x-direction of a control node (*CN*) which is a node common to both faces F_{X1} and F_{Y1}.

Y_{NODE} is the nodal position of the node and Y_{SEG} is the length of the segment in the y-direction.

1.2 Mixed uniform boundary conditions

Mixed uniform boundary conditions are applied in a similar manner to KUBC, where a displacement is assigned to the faces of the segment. However, in this case boundary conditions are only assigned to the faces perpendicular to the loading direction and the other four faces are allowed to freely deform, meaning that the stresses on theses non-loaded faces are equal to zero while the strains are not equal to zero. In each loading case, the corners of the cube were constrained such that rotations about the axes were prevented.

1.3 Static uniform boundary conditions

Static uniform boundary conditions are assigned by imposing opposing stresses on the faces perpendicular to the loading direction, or in the case of shear stress on the faces perpendicular to the two components of the loading direction. In this case, deformation is not restricted meaning that the stresses on non-loaded faces are equal to zero while the strains are not equal to zero. In each loading case, the corners of the cube were constrained such that rotations about the axes were prevented.

Appendix B

2 Calculation of effective isotropic elastic constants

2.1 Calculation of effective isotropic elastic constants

In order to generate effective isotropic elastic constants (E_{eff} and ν_{eff}) for each micromechanical segment model, the strain energy density (U) for each deformed configuration was calculated using:

$$U = \frac{1}{2}(\sigma_{11}\varepsilon_{11} + \sigma_{22}\varepsilon_{22} + \sigma_{33}\varepsilon_{33} + \sigma_{12}\gamma_{12} + \sigma_{23}\gamma_{23} + \sigma_{31}\gamma_{31}) \quad \text{(B.1)}$$

In Equation B.1 σ_{11} is the volume average stress in the (1) direction, σ_{12} is the volume average shear stress in the (1-2) plane, ε_{11} is the volume average strain in the (1) direction and γ_{12} is the volume average shear strain in the (1-2) plane with $\gamma_{12}=2\varepsilon_{12}$. This can then be related to the constitutive equations for a linear elastic material for an applied strain (Case 1) or an applied stress (Case 2) as per Bower et al. [60].

Case 1:

The constitutive equations for a linear elastic material for the case of an applied strain, where the volume averaged stress ‹$\boldsymbol{\sigma}$› can be calculated as a function of volume averaged strain ‹$\boldsymbol{\varepsilon}$›, E_{eff} and ν_{eff}, are described by Equation B.2.

$$\begin{bmatrix}\sigma_{11}\\ \sigma_{22}\\ \sigma_{33}\\ \sigma_{12}\\ \sigma_{23}\\ \sigma_{31}\end{bmatrix} = \frac{E_{\text{eff}}}{(1+v_{\text{eff}})(1-2v_{\text{eff}})}\begin{bmatrix} 1-v_{\text{eff}} & v_{\text{eff}} & v_{\text{eff}} & 0 & 0 & 0 \\ v_{\text{eff}} & 1-v_{\text{eff}} & v_{\text{eff}} & 0 & 0 & 0 \\ v_{\text{eff}} & v_{\text{eff}} & 1-v_{\text{eff}} & 0 & 0 & 0 \\ 0 & 0 & 0 & \frac{1-2v_{\text{eff}}}{2} & 0 & 0 \\ 0 & 0 & 0 & 0 & \frac{1-2v_{\text{eff}}}{2} & 0 \\ 0 & 0 & 0 & 0 & 0 & \frac{1-2v_{\text{eff}}}{2} \end{bmatrix}\begin{bmatrix}\varepsilon_{11}\\ \varepsilon_{22}\\ \varepsilon_{33}\\ \gamma_{12}\\ \gamma_{23}\\ \gamma_{31}\end{bmatrix} \quad \text{(B.2)}$$

By rearranging Equation B.1 and equating to the Equation B.2 for the specific loading case, E_{eff} can be re-written as a function of strain energy density, v_{eff} and strain, giving Equation B.3 for the case of uniaxial tension and Equation B.4 for simple shear. Directional variation in mechanical properties is accounted for by the isotropic modulus E_{eff} and Poisson's ratio v_{eff} by averaging strain energy density and strain. Here, U_{uniax} is the average of U_{11}, U_{22} and U_{33} where U_{11} is the strain energy density for uniaxial tensile loading in the (1) direction, etc., and U_{shear} is the average of U_{12}, U_{23} and U_{31} where U_{12} is the strain energy density for shear loading in the (1-2) plane, etc. Similarly, ε is the average of ε_{11} ε_{22} and ε_{33} and γ is the average of γ_{12}, γ_{23} and γ_{31}. Equations B.3 and B.4 below can be equated to solve for v_{eff}, giving Equation B.5. The Poisson's ratio v_{eff} can then be substituted back into Equation B.3 or B.4 to solve for E_{eff}.

$$E_{\text{eff}} = \frac{2U_{\text{uniax}}}{\varepsilon^2}\frac{(1+v_{\text{eff}})(1-2v_{\text{eff}})}{(1-v_{\text{eff}})} \quad \text{(B.3)}$$

$$E_{\text{eff}} = \frac{4U_{\text{shear}}}{\gamma^2}(1+v_{\text{eff}}) \quad \text{(B.4)}$$

$$v_{\text{eff}} = \frac{\left(\frac{2U_{\text{shear}}}{\gamma^2} - \frac{U_{\text{uniax}}}{\varepsilon^2}\right)}{\left(\frac{2U_{\text{shear}}}{\gamma^2} - \frac{2U_{\text{uniax}}}{\varepsilon^2}\right)} \quad \text{(B.5)}$$

Case 2:

The constitutive equations for a linear elastic material for the case of an applied stress, where ‹$\boldsymbol{\varepsilon}$› can be calculated as a function of ‹$\boldsymbol{\sigma}$›, E_{eff} and v_{eff}, are described by Equation B.6.

$$\begin{bmatrix}\varepsilon_{11}\\ \varepsilon_{22}\\ \varepsilon_{33}\\ \gamma_{12}\\ \gamma_{23}\\ \gamma_{31}\end{bmatrix} = \frac{1}{E_{\text{eff}}}\begin{bmatrix}1 & -v_{\text{eff}} & -v_{\text{eff}} & 0 & 0 & 0\\ -v_{\text{eff}} & 1 & -v_{\text{eff}} & 0 & 0 & 0\\ -v_{\text{eff}} & -v_{\text{eff}} & 1 & 0 & 0 & 0\\ 0 & 0 & 0 & 2(1+v_{\text{eff}}) & 0 & 0\\ 0 & 0 & 0 & 0 & 2(1+v_{\text{eff}}) & 0\\ 0 & 0 & 0 & 0 & 0 & 2(1+v_{\text{eff}})\end{bmatrix}\begin{bmatrix}\sigma_{11}\\ \sigma_{22}\\ \sigma_{33}\\ \sigma_{12}\\ \sigma_{23}\\ \sigma_{31}\end{bmatrix} \tag{B.6}$$

By rearranging B.1 and setting it equal to Equation B.6 for the relevant loading case, E_{eff} can be re-written as a function of strain energy density, v_{eff} and strain, as demonstrated for the cases of uniaxial tension using Equation B.7 and simple shear using Equation B.8 below. U_{uniax} and U_{shear} are as per Case 1, σ_{uniax} is the average of σ_{11}, σ_{22} and σ_{33} and σ_{shear} is the average of σ_{12}, σ_{23} and σ_{31}. Equations B.7 and B.8 can be equated to solve for v_{eff}, giving Equation B.9. The Poisson's ratio v_{eff} can then be substituted back into Equation B.7 or B.8 to solve for E_{eff}.

$$E_{\text{eff}} = \frac{\sigma_{\text{uniax}}^2}{U_{\text{uniax}}}(1+v_{\text{eff}}) \tag{B.7}$$

$$E_{\text{eff}} = \frac{\sigma_{\text{shear}}^2}{2U_{\text{shear}}} \tag{B.8}$$

$$v_{\text{eff}} = \frac{\frac{\sigma_{\text{uniax}}^2}{2U_{\text{uniax}}} - \frac{\sigma_{\text{shear}}^2}{U_{\text{shear}}}}{\frac{\sigma_{\text{shear}}^2}{U_{\text{shear}}}} \tag{B.9}$$

3 Tables and Figures

Table 1: Literature survey of mechanical properties of PCL[9,13,14,31,39,42,45,52,57]

Material source	***E*** **(MPa)**	M_w	**Fabrication**	**Sources**
CAPA 6501, Solvay	122	50,000	SLS	57
CAPA 6501, Solvay	297.8	50,000	SLS	13
CAPA 6501, Solvay	299	50,000	SLS	14
CAPA 6501, Solvay	120	50,000	Material datasheet	57
CAPA 6501, Solvay	645.88	50,000	Vacuum melting	45
CAPA 6506, Solvay	320	50,000	Extrusion	31
Sigma-Aldrich	250	65,000	Drop-on-demand printer	39
Sigma-Aldrich	300	65,000	Melt pressing	52
Sigma-Aldrich	373	80,000	Solvent casting, film pressing	42
Sigma-Aldrich	400	80,000	Melt blending & pressing	9

Table A.1: Boundary conditions used for the assignment of kinematic, static, and mixed uniform boundary conditions

	Direction	F_{x0}	F_{x1}	F_{y0}	F_{y1}	F_{z0}	F_{z1}
KUBC							
Uniaxial strain	1	$\varepsilon_{11} = 0$	$\varepsilon_{11} = \varepsilon$	$\varepsilon_{22} = 0$	$\varepsilon_{22} = 0$	$\varepsilon_{33} = 0$	$\varepsilon_{33} = 0$
	2	$\varepsilon_{11} = 0$	$\varepsilon_{11} = 0$	$\varepsilon_{22} = 0$	$\varepsilon_{22} = \varepsilon$	$\varepsilon_{33} = 0$	$\varepsilon_{33} = 0$
	3	$\varepsilon_{11} = 0$	$\varepsilon_{11} = 0$	$\varepsilon_{22} = 0$	$\varepsilon_{22} = 0$	$\varepsilon_{33} = 0$	$\varepsilon_{33} = \varepsilon$
Simple shear	1–2	$\varepsilon_{11} = f(\varepsilon)$	$\varepsilon_{11} = f(\varepsilon)$	$\varepsilon_{11} = 0$, $\varepsilon_{22} = 0$	$\varepsilon_{11} = \varepsilon$, $\varepsilon_{22} = 0$	$\varepsilon_{33} = 0$	$\varepsilon_{33} = 0$
	2–3	$\varepsilon_{11} = 0$	$\varepsilon_{11} = 0$	$\varepsilon_{22} = f(\varepsilon)$	$\varepsilon_{22} = f(\varepsilon)$	$\varepsilon_{22} = 0$, $\varepsilon_{33} = 0$	$\varepsilon_{22} = \varepsilon$, $\varepsilon_{33} = 0$
	3–1	$\varepsilon_{33} = 0$, $\varepsilon_{11} = 0$	$\varepsilon_{33} = \varepsilon$, $\varepsilon_{11} = 0$	$\varepsilon_{22} = 0$	$\varepsilon_{22} = 0$	$\varepsilon_{33} = f(\varepsilon)$	$\varepsilon_{33} = f(\varepsilon)$
MUBC							
Uniaxial strain	1	$\varepsilon_{11} = 0$	$\varepsilon_{11} = \varepsilon$	–	–	–	–
	2	–	–	$\varepsilon_{22} = 0$	$\varepsilon_{22} = \varepsilon$	–	–
	3	–	–	–	–	$\varepsilon_{33} = 0$	$\varepsilon_{33} = \varepsilon$
Shear	1–2	–	–	$\varepsilon_{11} = 0$	$\varepsilon_{11} = \varepsilon$	–	–
	2–3	–	–	–	–	$\varepsilon_{22} = 0$	$\varepsilon_{22} = \varepsilon$
	3–1	$\varepsilon_{33} = 0$	$\varepsilon_{33} = \varepsilon$		–	–	–
SUBC							
Uniaxial stress	1	$\sigma_{11} = -\sigma$	$\sigma_{11} = \sigma$	–	–	–	–
	2	–	–	$\sigma_{22} = -\sigma$	$\sigma_{22} = \sigma$	–	–
	3	–	–	–	–	$\sigma_{33} = -\sigma$	$\sigma_{33} = \sigma$
Shear	1–2	$\sigma_{22} = -\sigma$	$\sigma_{22} = \sigma$	$\sigma_{11} = -\sigma$	$\sigma_{11} = \sigma$	–	–
	2–3	–	–	$\sigma_{33} = -\sigma$	$\sigma_{33} = \sigma$	$\sigma_{22} = -\sigma$	$\sigma_{22} = \sigma$
	3–1	$\sigma_{33} = -\sigma$	$\sigma_{33} = \sigma$	–	–	$\sigma_{11} = -\sigma$	$\sigma_{11} = \sigma$

Here, ε_{11} is strain in the positive *x*-direction, σ_{11} is stress in the positive *x*-direction, ε is the magnitude of the applied strain, and σ is the magnitude of the applied stress

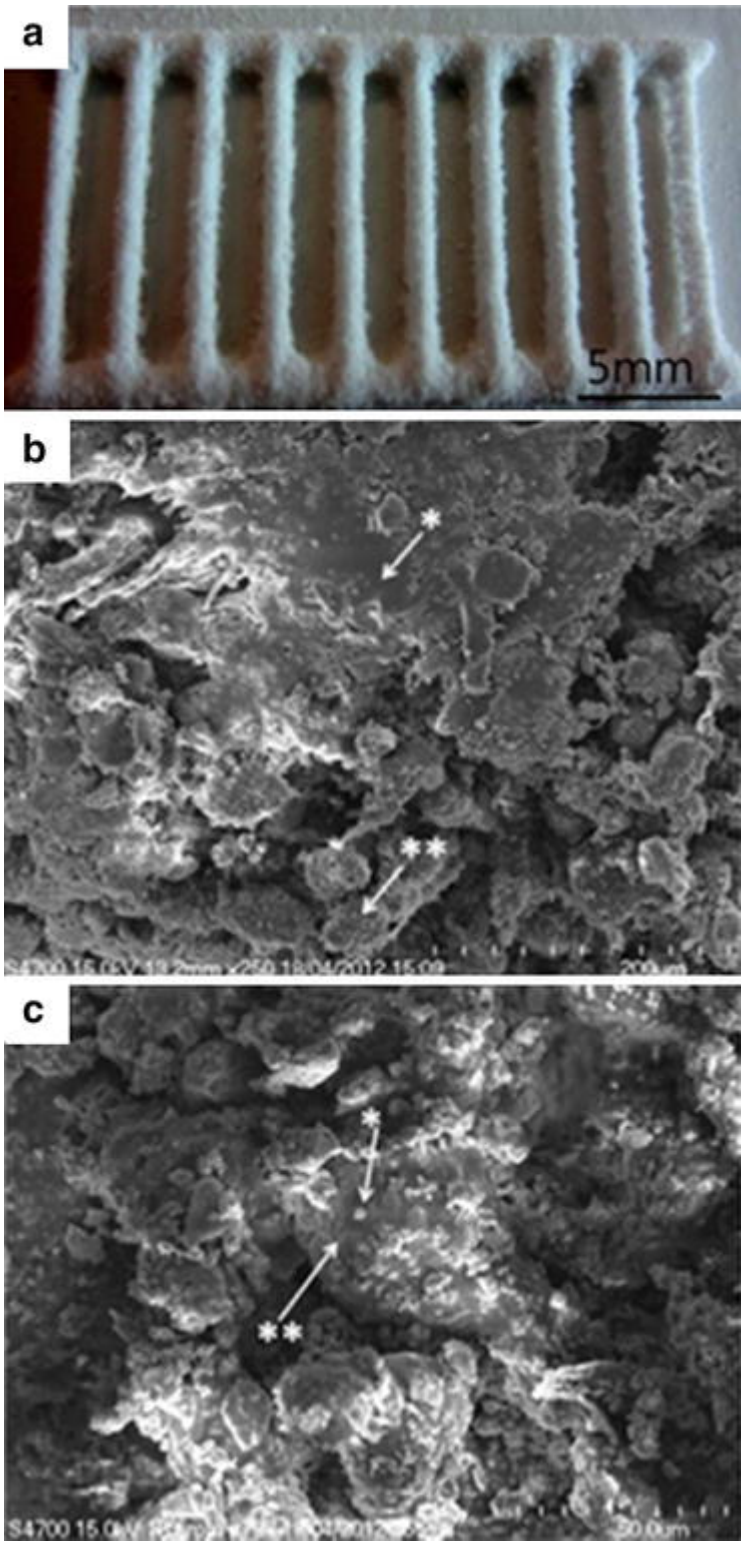

Figure 1: Selective laser sintered strut ladder (a). SEM images of the PCL/β-TCP scaffolds showing areas of fully sintered material (*) and partially sintered material (**) (b). A higher magnification image (c) shows β-TCP (*) and PCL (**)

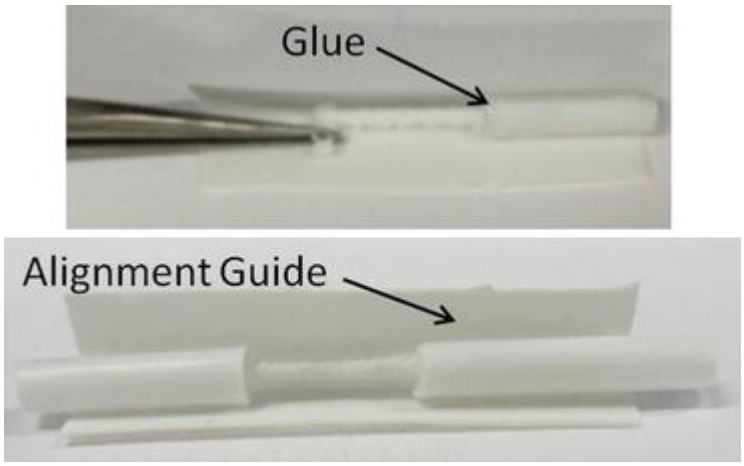

Figure 2: Preparation of tensile test specimens from single struts

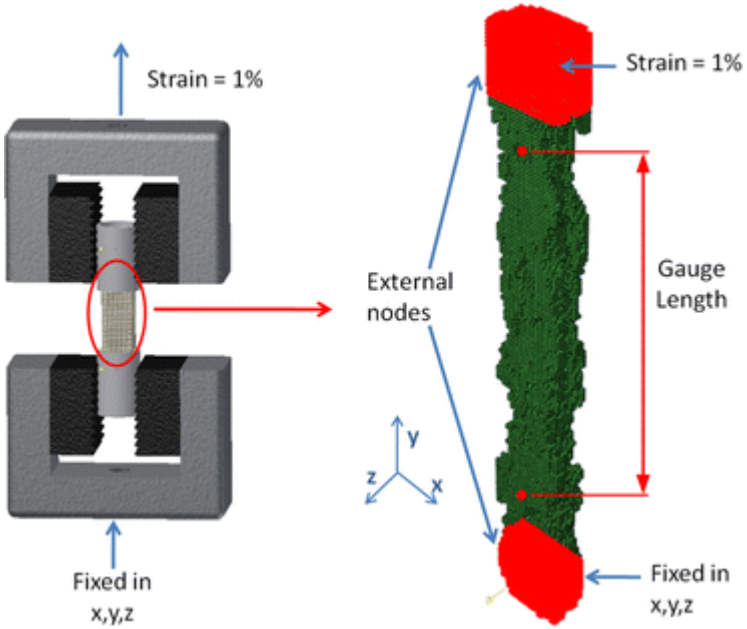

Figure 3: Schematic diagram of tensile test set-up for single strut testing (left) and FE model set-up for tensile test simulation (right)

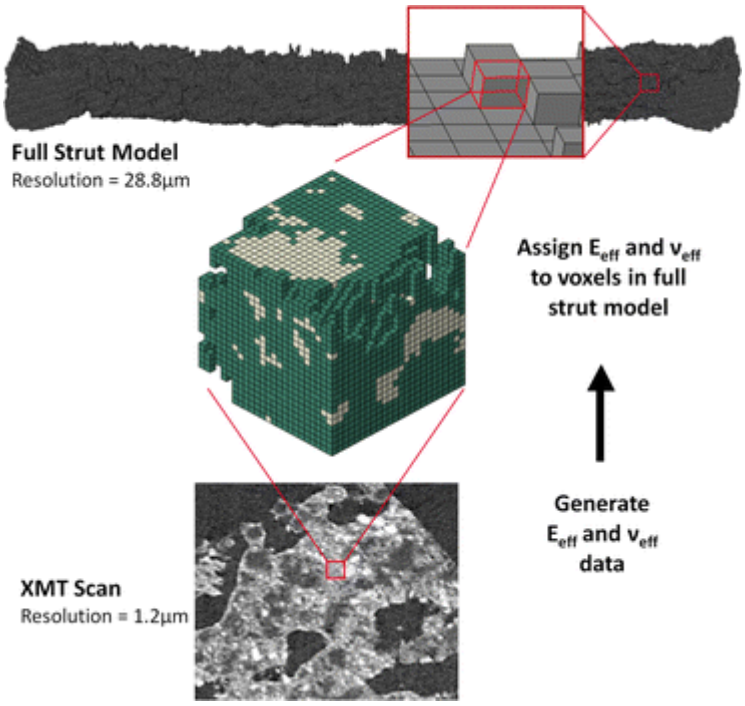

Figure 4: Micromechanical models are used to generate E_{eff} data, which is then used to assign individual specific element mechanical properties based on average element grey-value

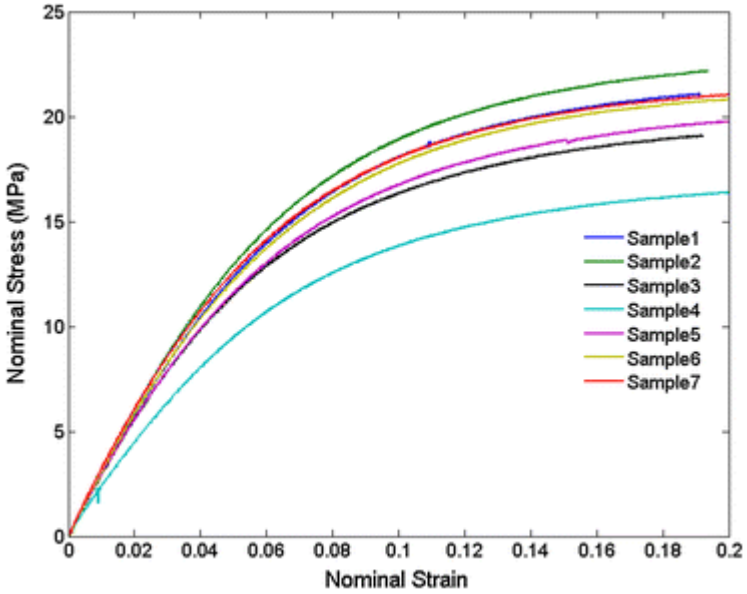

Figure 5: Tensile curves for pure PCL samples tested to 0.2 strain

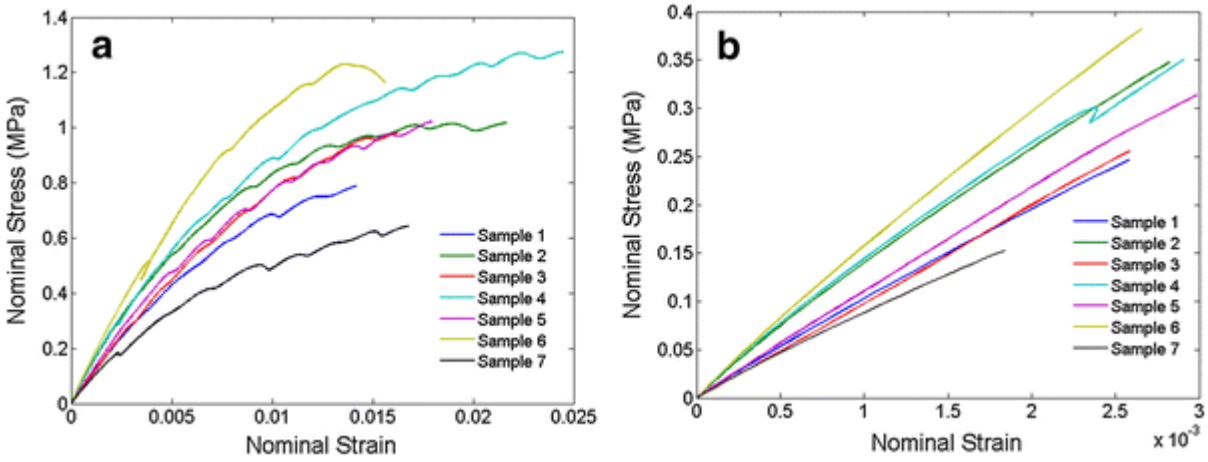

Figure 6: Tensile curves for sintered struts tested to failure, with n = 7 (a). Expanded view of the linear region of tensile curves for evaluation of elastic modulus (b)

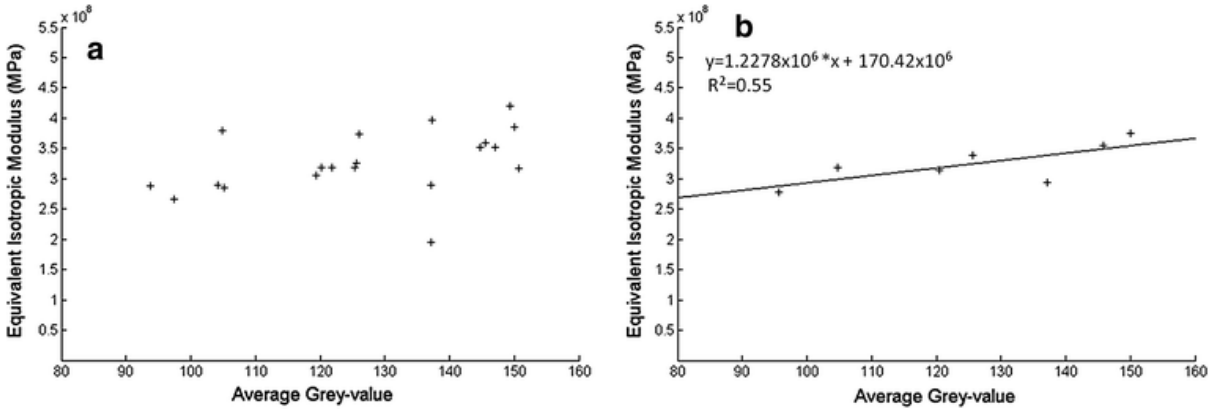

Figure 7: Variation of E_{eff} with average grey-value with multiple segments for each grey-value (a) and variation of grey-value averaged E_{eff} with average grey-value (b), both for the second phase of model development

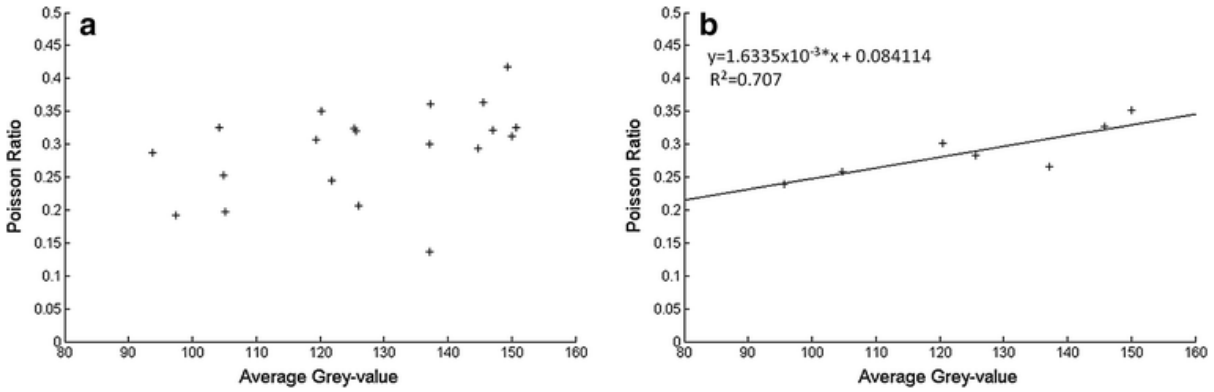

Figure 8: Variation of Poisson's ratio (v_{eff}) with average segment grey-value with multiple segments for each grey-value (a) and variation of grey-value averaged v_{eff} with average segment grey-value (b), both for the second phase of model development

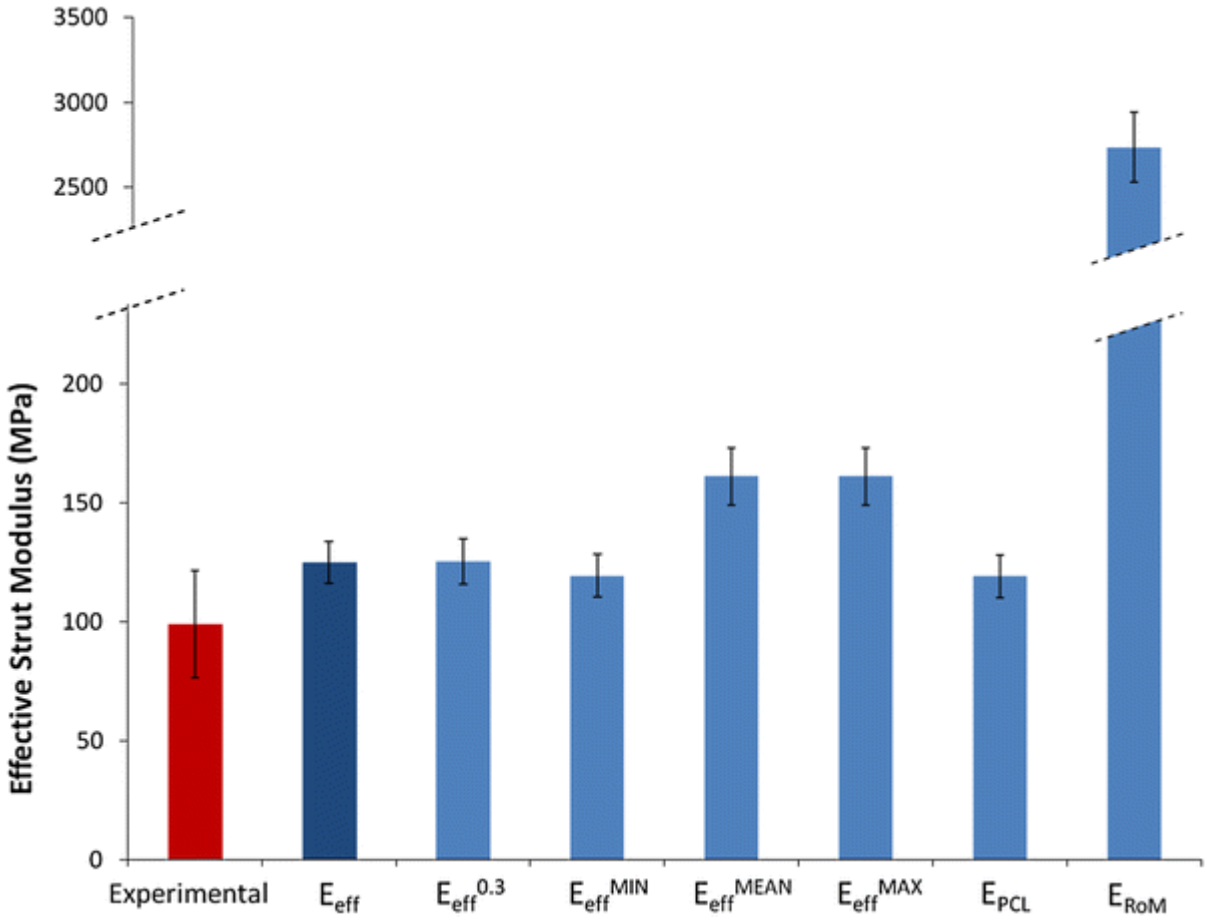

Figure 9: Comparison of experimental (red, $n = 7$) and computationally evaluated (blue, $n = 4$) strut effective moduli for different methods of material assignment, with input material property type indicated on the x-axis. E_{eff} uses heterogeneous assignment of E_{eff} and v_{eff}, while $E_{\text{eff}}^{0.3}$ uses heterogeneous assignment of E_{eff} and a constant Poisson's ratio of 0.3. $E_{\text{eff}}^{\text{MIN}}$, $E_{\text{eff}}^{\text{MEAN}}$, and $E_{\text{eff}}^{\text{MAX}}$ use homogeneous assignment of the minimum, mean, and maximum values of E_{eff}, respectively, each with a constant Poisson's ratio of 0.3. E_{PCL} and E_{RoM} use homogeneous assignment of the elastic modulus of PCL and a composite modulus calculated using the RoM, respectively, with a constant Poisson's ratio of 0.3. Note that the plot is shown with a broken y-axis in order to show the RoM result on the same plot as the experimental results

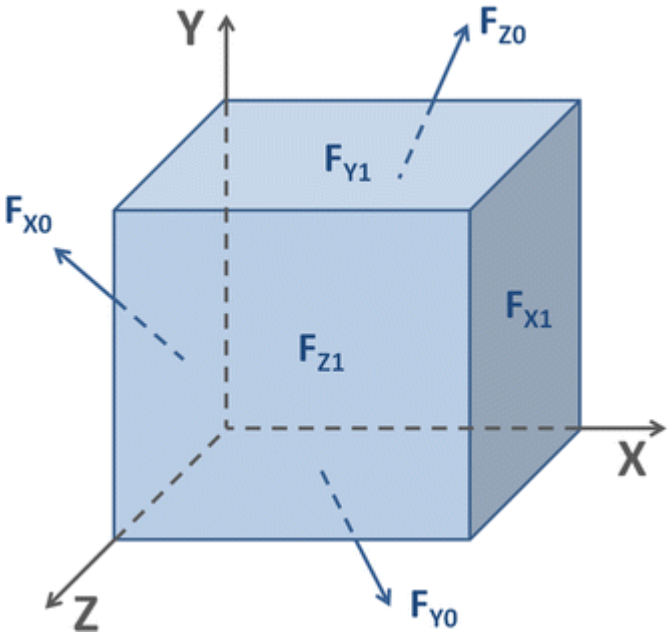

Figure A.1: Notation used to describe the faces of a cube segment for the application of uniform boundary conditions discussed in Appendix A

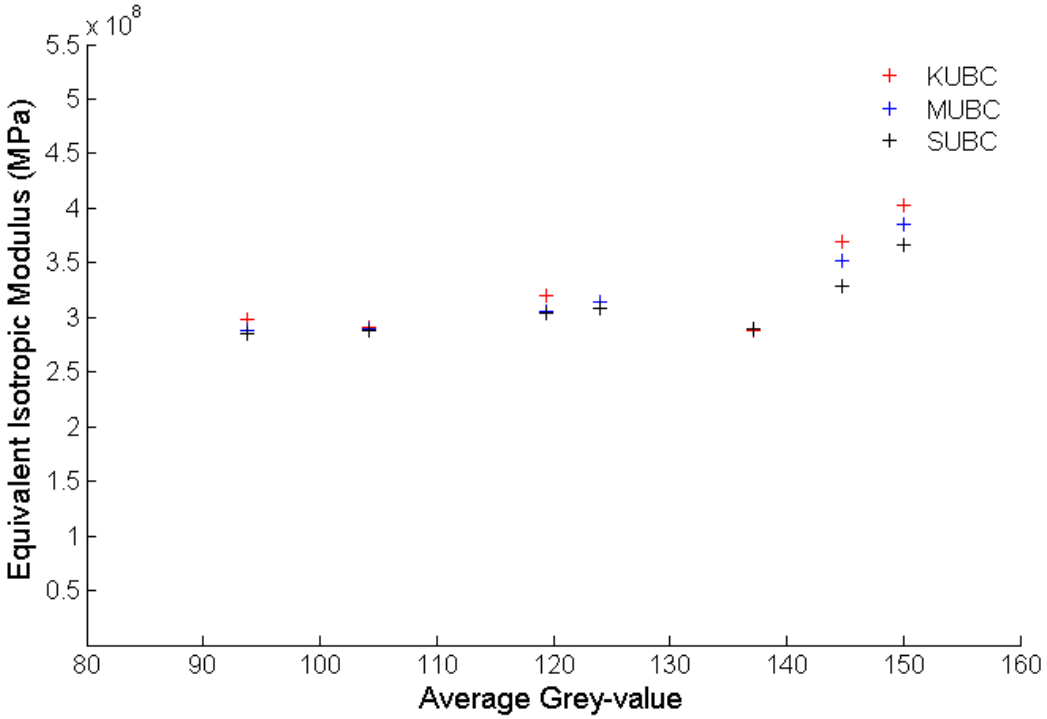

Figure S1: E_{eff} plotted against average segment grey-value for segments in the first phase of model development.

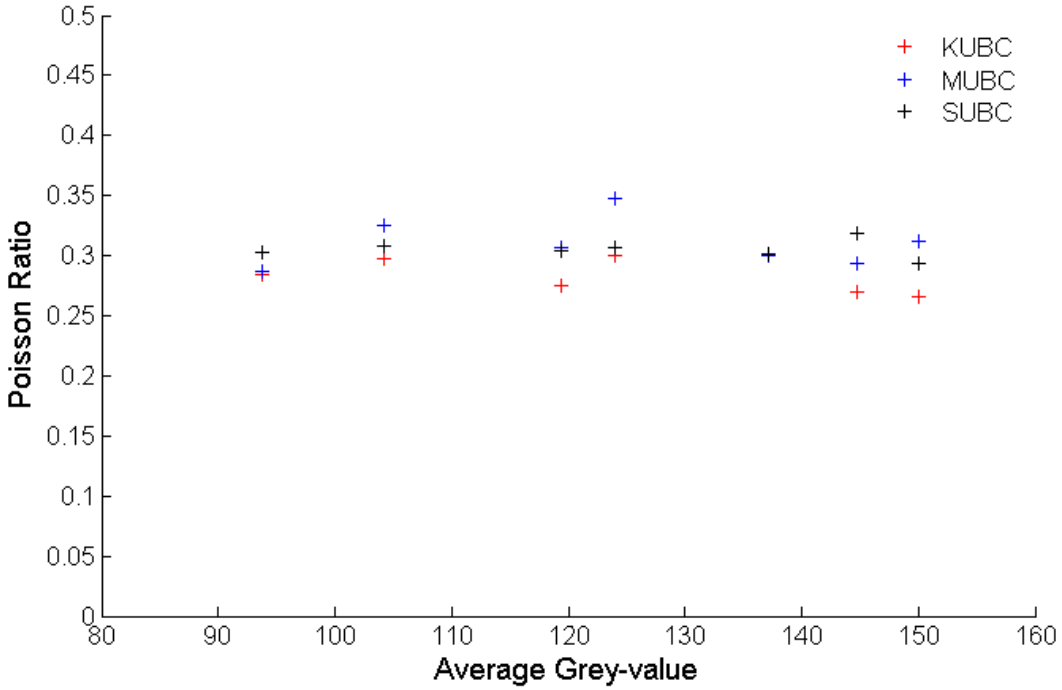

Figure S2: Poisson's ratio ν_{eff} plotted against average segment grey-value for segments in the first phase of model development

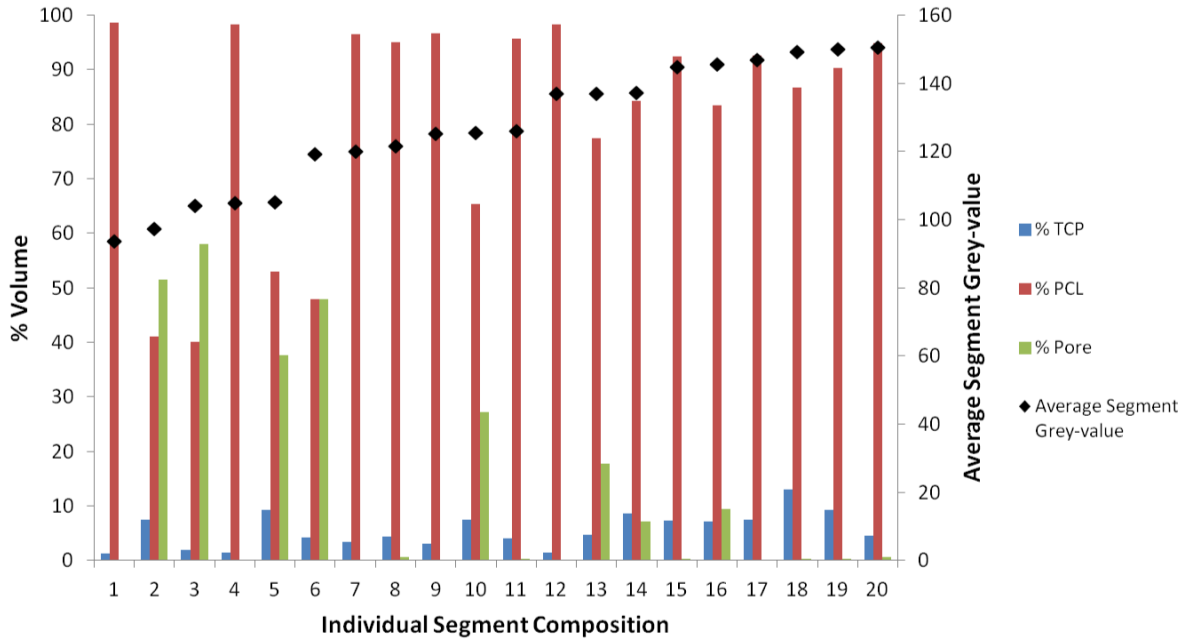

Figure S3: Segment material composition and average segment grey-value for segments in the second phase of model development